Unconventional Nonlinear Hall Effects in Twisted Multilayer 2D Materials

Mahmut Sait Okyay[1], Min Choi[1], Qiang Xu[1], Adrián Perez Diéguez[2], Mauro Del Ben[2], Khaled Z. Ibrahim[2], and Bryan M. Wong[*,1]

1 *Department of Chemistry, Department of Physics & Astronomy, and Materials Science & Engineering Program, University of California-Riverside, Riverside, California 92521, United States*

2 *Applied Mathematics & Computational Research Division, Lawrence Berkeley National Laboratory, Berkeley, California 94720, United States*

*E-mail: bryan.wong@ucr.edu, Website: http://www.bmwong-group.com

ABSTRACT

We present the first investigation of unusual nonlinear Hall effects in twisted multilayer 2D materials. Contrary to expectations, our study shows that these nonlinear effects are not merely extensions of their monolayer counterparts. Instead, we find that stacking order and pairwise interactions between neighboring layers, mediated by Berry curvatures, play a pivotal role in shaping their collective nonlinear optical response. By combining large-scale Real-Time Time-Dependent Density Functional Theory (RT-TDDFT) simulations with model Hamiltonian analyses, we demonstrate a remarkable second-harmonic transverse response in hexagonal boron nitride four-layers, even in cases where the total Berry curvature cancels out. Furthermore, our symmetry analysis of the layered structures provides a simplified framework for predicting nonlinear responses in multilayer materials in general. Our investigation challenges the prevailing understanding of nonlinear optical responses in layered materials and opens new avenues for the design and development of advanced materials with tailored optical properties.

Significance statement: Our findings advance the fundamental understanding of nonlinear optical phenomena in twisted multilayer 2D materials and offer a path toward designing controllable optoelectronic devices by manipulating their stacking configurations.

I. INTRODUCTION

Nonlinear optical phenomena in two-dimensional (2D) materials have garnered significant attention due to their potential applications in next-generation optoelectronic and photonic devices [1-4]. Among these materials, hexagonal boron nitride (h-BN), with its wide band gap and robust mechanical properties, has emerged as a promising platform for investigating new physical phenomena and enhancing device functionalities [5-9]. A particularly unique property in these materials is the nonlinear Hall effect, typically a second-order transverse response driven by the Berry curvature dipole in non-centrosymmetric non-magnetic systems [10-14]. This effect has been extensively documented in monolayers and simple bilayers, yet its complexity significantly increases with additional stacking configurations [15-23].

Recent advancements have shown that multilayer configurations of 2D materials exhibit unique electronic and optical properties that are not merely extensions of their monolayer counterparts [24-29]. Specifically, the interaction between layers and the resulting modification of physical properties due to stacking configurations offer a rich landscape for the exploration of novel phenomena, such as superconducting flat bands in bilayer graphene with Moire patterns, induction of spin-orbit coupling, and controllable film growth mechanisms [30-33]. However, conventional theories that describe the nonlinear Hall effect based on the total Berry curvature dipole are insufficient for multilayer structures where interlayer dynamics significantly influence the overall effect.

This study examines the unusual and unexpected behavior of the nonlinear Hall effect within stacked multilayer structures. Our results show that beyond the conventional Berry curvature dipole model, the stacking order and interlayer interactions are crucial in dictating the nonlinear optical responses of these systems. Using state-of-the-art theoretical methods, including Real-Time Time-Dependent Density Functional Theory (RT-TDDFT) [34-38], model Hamiltonian approaches, and symmetry analysis, we dissect the contributions of interlayer interactions and uncover the underlying mechanisms of the nonlinear Hall effect in h-BN multilayers. In contrast to traditional approaches, our results show a unique second-harmonic transverse response in twisted h-BN four-layers despite the nullification of the overall Berry curvature. We observe distinct nonlinear optical properties due to different chiral stacking configurations and propose a novel method to control optical responses using directional torsion forces. Our investigation challenges the prevailing understanding of the topological origin of the optical nonlinear Hall responses in layered materials and opens new avenues for the design and development of advanced materials with tailored optical properties.

II. RESULTS

A. Theory and construction of twisted h-BN multilayers.

The relationship between the nonlinear Hall response of insulators and their Berry curvatures was recently explored by one of us [11]. In this previous study, the main contribution to the second-harmonic Hall current density $\mathbf{J}_{\perp}^{2\omega}$ of a non-centrosymmetric insulator to an applied electric field $\mathbf{E}$ with frequency ω was found to be proportional to the Berry curvature dipole as

$$\mathbf{J}_{\perp}^{2\omega} \approx -\frac{2\pi e^3}{\hbar^2 \omega} \hat{\mathbf{z}} \times \mathbf{E} \sum_{nm} f_{n\mathbf{k}} (1 - f_{m\mathbf{k}}) \mathbf{D}_{nm} \cdot \mathbf{E}, \quad (1)$$

where e is the charge of an electron, $\hat{\mathbf{z}}$ is the normal unit vector of the 2D material surface, and $f_{n\mathbf{k}}$ are the band occupation factors. $\mathbf{D}_{nm}$ are the interband Berry curvature dipole matrix

elements between band *n* and band *m*, defined as

$$\mathbf{D}_{nm}(\omega) = \int_{\mathbf{k}} \frac{\partial \Omega_{nm}}{\partial \mathbf{k}} \Theta(2\omega - \omega_{mn}), \tag{2}$$

where $\int_{\mathbf{k}} \equiv \int \frac{d^2\mathbf{k}}{4\pi^2}$ represents the 2D Brillouin zone integration, $\omega_{mn} = [\varepsilon_m(\mathbf{k}) - \varepsilon_n(\mathbf{k})]/\hbar$ is the energy-level difference between the ground state eigenstates $|\psi_m(\mathbf{k})\rangle$ and $|\psi_n(\mathbf{k})\rangle$ at a crystal momentum point $\mathbf{k}$, Θ is the Heaviside step function, and Ω_{nm} is the interband Berry curvature [11] given by

$$\Omega_{nm}(\mathbf{k}) = 2\mathrm{Im}\frac{v_{nm}^{y} v_{mn}^{x}}{\omega_{mn}^{2}}, \tag{3}$$

where v_{nm}^{y} and v_{nm}^{x} are the *y*- and *x*-components of the dipole matrix elements $\langle\psi_n(\mathbf{k})|\hat{\mathbf{p}}|\psi_m(\mathbf{k})\rangle$, respectively, where $\hat{\mathbf{p}}$ denotes the momentum operator.

Using the identity between the total interband and total single-band Berry curvatures $\sum_{nm} f_{n\mathbf{k}}(1 - f_{m\mathbf{k}})\Omega_{nm} = \sum_n f_{n\mathbf{k}}\Omega_n$, where the single-band Berry curvature is $\Omega_n(\mathbf{k}) = 2\mathrm{Im}\sum_{m\neq n} v_{nm}^{y} v_{mn}^{x}/\omega_{mn}^{2}$, we obtain the following qualitative relationship

$$\mathbf{J}_{\perp}^{2\omega} \propto \sum_n \oint_{\mathbf{k}} \frac{\partial \Omega_n}{\partial \mathbf{k}}, \tag{4}$$

where the integration is performed over the area enclosed by $\Theta(2\omega - \omega_{vc})$, and the bandgap of the system is the energy separation between *v* (valence band maximum, VBM) and *c* (conduction band minimum, CBM). The integration area in Eq. (2) is determined separately for *n*-*m* band pairs, and, thus, Eq. (4) can have fewer or more terms than Eq. (1). However, our approximation in Eq. (4) is valid since the main contribution to the Berry curvature arises from VBM and CBM bands [11]. The term "Berry curvature" represents the total single-band Berry curvature hereafter.

We argue that the second-harmonic Hall current of two distinct systems, whose band structures are very similar and momentum-resolved Berry curvatures are proportional to each other, can directly be compared by their total Berry curvatures at any arbitrary $\mathbf{k}$ point:

$$\mathbf{J}_{\perp}^{2\omega} \propto \sum_n \Omega_n. \tag{5}$$

This argument holds for some special cases, such as homogenous Van der Waals multilayer structures whose Berry curvatures are summative/additive. In these structures, comparing the Berry curvature at an arbitrary $\mathbf{k}$ point is enough to compare their integrated Berry curvature. From this approximation, we comprehensively include the contributions of higher-order Berry curvature multipoles [39] with the dipole, as their magnitudes are also proportional to the magnitude of the Berry curvature.

We found that the use of Eq. (5) is suitable for the description of the 2D systems in this work [11]. Therefore, we analyze the second-harmonic Hall response of twisted h-BN multilayers under a linearly polarized laser field with nearly half the bandgap frequency that maximizes the transverse second-harmonic generation (see Fig. 1). Each layer exhibits a second-harmonic response in the transverse direction (gray arrows in Fig. 1) depending on its Berry curvature component that connects the directions of the field and its response. For instance, we calculate Ω^{xy} since the applied field is polarized in the *x*-direction and the corresponding response is polarized in the *y*-direction.

To construct the twisted h-BN multilayers, we first define the twist angle and possible monolayers in the supercell of the corresponding twist angle. The smallest twisted supercell for a hexagonal unit cell is a $\sqrt{7} \times \sqrt{7}$ supercell that corresponds to a 21.8˚ twist angle [40, 41] (see Methods for further details on geometry optimizations and other calculation parameters). There are four possible configurations of a h-BN monolayer on a $\sqrt{7} \times \sqrt{7}$ supercell: A, A', B, and B', as shown in Fig. 2. Configurations A and B are inversion pairs such that B can be obtained by an inversion transformation of A or simply by flipping the position of boron and nitrogen bases. This transformation also flips the sign of the Berry curvature. Thus, if the Berry curvature of A at a certain $\mathbf{k}$ point is Ω, it is $-\Omega$ for B. Similarly, A' and B' configurations are obtained by mirror reflection of A and B with respect to the *yz*-plane. This

reflection also results in a flip in the sign of the Berry curvatures. On the other hand, A-B' and A'-B are reflection pairs with respect to the *xz*-plane and have Berry curvatures with the same sign. Therefore, the Berry curvature of configurations A and B' is Ω, whereas it is $-\Omega$ for A' and B (see Fig. 2). The three-fold symmetry of the individual h-BN layers dictates three identical Berry curvature dipoles, $\mathbf{D}_{nm}$, with a 120° angle separation, resulting in the cancellation of the Berry curvature contribution to the second-harmonic Hall effect, as can be obtained from summation of $\mathbf{D}_{nm}$ along different directions through Eq. (1). However, in this study, we focus on stacked multilayers that do not preserve three-fold symmetry. Therefore, the Berry curvatures of individual layers contribute without cancellation to the system's total Berry curvature dipole.

We investigated whether a specific stacking order of twisted layers can bring unusual phenomena, such as chirality-dependent optical effects [42, 43], chiral-torsion effects [44], or torsion-induced transport [45]. For this purpose, we prepared clockwise-twisted (CW-twisted) and counterclockwise-twisted (CC-twisted) multilayers separated by a ~3.5 Å distance. Since none of the allowed twist angles for constructing a moiré lattice are integer multiples that can divide 120˚, it is impossible to achieve uniformly twisted multilayers [40]. However, we can mimic CW- and CC-twisted structures with AA'BB' and AB'BA' stacking, as seen in Fig. 3. In this case, the twist angle between the 1st and 2nd layers in the CW-twisted ordering (A and A') is 21.8˚, whereas it is 38.2˚ between the 2nd and 3rd layers (A' and B). Even though we cannot obtain a uniform twisting between neighboring layers due to a non-integer twist angle, alternating stacking of layers with a 30˚±8.2˚ angle would effectively produce twisted structures.

B. Berry curvature and second-order optical responses of twisted h-BN multilayers

We compare the total Berry curvatures and second-harmonic Hall responses for monolayer,

bilayers, 3-layers, and 4-layers of CW- and CC-twisted stackings of h-BN. This comparison allows us to assess whether (1) the Berry curvature of multilayers is additive, (2) twisted stackings provide novel phenomena, and (3) real-time current responses maintain the quantized behavior of the Berry curvature.

The momentum-resolved total Berry curvatures of the 1- to 4-layer structures are given in Fig. 4. We denote the Berry curvature of the monolayer (configuration A) at the $\mathbf{k} = \mathrm{K}$ point as Ω (see black dashed line in Fig. 4a) and compare the Berry curvatures at the same $\mathbf{k}$-point for the other multilayers. The additive behavior of the Berry curvature can be observed in Figs. 4b and 4c. The stacking in the CW- and CC-twisted systems are (A, A', B, B') and (A, B', B, A'), and their Berry curvatures are $(\Omega, -\Omega, -\Omega, \Omega)$ and $(\Omega, \Omega, -\Omega, -\Omega)$, respectively. The summation of the individual Berry curvatures of mono-, bi-, 3-, and 4-layers of CW- and CC-twisted stackings are $(\Omega, \Omega - \Omega, \Omega - \Omega - \Omega, \Omega - \Omega - \Omega + \Omega) = (\Omega, 0, -\Omega, 0)$ and $(\Omega, \Omega + \Omega, \Omega + \Omega - \Omega, \Omega + \Omega - \Omega - \Omega) = (\Omega, 2\Omega, \Omega, 0)$, respectively. As seen in Figs. 4b and 4c, the calculated total Berry curvatures of the multilayers show the exact same values. Therefore, we can conclude that the Berry curvature of h-BN multilayers is summative; i.e., the total Berry curvature of the system is the summation of each layer's Berry curvature.

To compare the Berry curvatures obtained from the ground-state wavefunctions with real-time excited-state responses, we carried out RT-TDDFT calculations that explicitly propagate the excited-state wavefunctions in real time [36]. The Kohn–Sham (KS) wavefunctions $|\psi_{n\mathbf{k}}(\mathbf{r}, t)\rangle$ are propagated via the time-dependent KS equation as follows:

$$i\hbar \frac{\partial}{\partial t} |\psi_{n\mathbf{k}}(\mathbf{r}, t)\rangle = \left[\frac{1}{2m_e} \left(\hat{\mathbf{p}} - \frac{e}{c} \mathbf{A}(t) \right)^2 + \hat{V}_{\mathrm{atom}} + \hat{V}_{\mathrm{Hxc}}[\rho(\mathbf{r}, t)] \right] |\psi_{n\mathbf{k}}(\mathbf{r}, t)\rangle, \qquad (6)$$

where the second and third terms within the brackets are the atomic pseudopotential and Hartree-exchange-correlation potential, respectively. m_e is the electron mass, c is the speed

of light, and the vector potential $\mathbf{A}(t) = -c\int_0^t d\tau \mathbf{E}(\tau)$ corresponds to the electric field component of the applied laser, $\mathbf{E}(t)$, which is polarized in the *x*-direction (see the upper panel of Fig. 5a) according to:

$$E_x(t) = E_0 \sin(\omega_0 t) \times \begin{cases} 3(t/20)^2 - 2(t/20)^3, & 0 < t \leq 20 \\ 1, & 20 < t \leq 40 \\ 1 - 3[(t-40)/20]^2 + 2[(t-40)/20]^3 & 40 < t \leq 60 \\ 0, & 60 < t \end{cases}, \quad (7)$$

where the laser strength and frequency is set to $E_0 = 0.01$ V/Å and $\omega_0 = 0.65\varepsilon_{\text{gap}}$, respectively, to maximize the nonlinear Hall response [11]. The details of our RT-TDDFT computations are provided in Methods. The cell-averaged transverse current density can be calculated from the velocity expectation value of the time-evolving KS wavefunctions:

$$J_y(t) = -\frac{e}{Lm_e}\sum_{n\mathbf{k}} f_{n\mathbf{k}} \langle \psi_{n\mathbf{k}}(\mathbf{r},t) | \hat{\pi}_y | \psi_{n\mathbf{k}}(\mathbf{r},t) \rangle, \quad (8)$$

where *L* is the average length of the 2D unit cell in the *y*-direction. The mechanical momentum operator in the velocity gauge is given by $\hat{\pi}_y = \hat{p}_y + \frac{m}{i\hbar}[r_y, \hat{V}_{\text{NL}}]$, where $\hat{V}_{\text{NL}}$ is the nonlocal part of the pseudopotential [46]. To minimize the numeric noise of the time evolution, we subtract the current response with $\mathbf{A}(t) = 0$ from the current response with the applied laser vector potential. Furthermore, to obtain a pure second-order response without odd-order contributions, we also calculate the response with $-\mathbf{A}(t)$ and add it to the response with $\mathbf{A}(t)$. (see Methods for more details.)

Taking the current density response of the monolayer in Fig. 5a as a reference, we observe that the bilayers in the left panels of Figs. 5b and 5c are consistent with the corresponding Berry curvatures presented in the left panels of Figs. 4b and 4c. The CW-twisted bilayer shows no response, while the CC-twisted bilayer exhibits enhanced response even if it is not ideally twice the monolayer response. The real-time dynamics of 3-layers are also consistent with the corresponding Berry curvatures: Ω and $-\Omega$ for CW- and CC-twisted 3-layers, respectively.

The real-time responses of the CW- and CC-twisted structures have opposite signs, as seen in the insets of the middle panels of Figs. 5b and 5c. Moreover, the magnitude of the current responses of 3-layer structures is similar to one of the monolayers (Fig. 5a). The average amplitudes and frequencies of the observed responses are presented in Figs. 5d-f. The CC-twisted bilayer exhibits a response with an amplitude approximately twice that of the monolayer and the 3-layer system. On the other hand, all non-zero responses show only the $2\omega_0$ frequency component, indicating that the obtained responses correspond exclusively to second-order Hall currents.

The CW- and CC-twisted stackings are different in terms of the evolution of the Berry curvature. However, these are natural outcomes of the summative behavior and are not unique to chiral ordering. Chiral structures are usually incorporated with magnetic effects such as chirality-induced spin selectivity [47, 48]. Since we only consider pure electron dynamics associated with the stacking of the structures without considering the spin degree of freedom nor explicitly including magnetic effects, it is expected that we do not reproduce any chirality-induced phenomena. Nevertheless, the distinct nonlinear responses depending on twisting direction suggest a novel engineering application: CW- and CC-twisted multilayers can be switched by applying an opposite torsional force to the slab structure. For instance, the nonlinear signal in the bilayer structure can be turned on and off only by rotating the layers in the opposite direction in the *xy*-plane by a torsion force. Similarly, the sign of the signals in 3 layers can be switched by the same structural manipulation. Collectively, these approaches introduce a new, previously unexplored technique for adjusting optical responses by applying directional torsion forces to these systems.

The situation is dramatically different for the 4-layer structures. The CW- and CC-twisted 4-layers have zero Berry curvature over the Brillouin zone. Thus, one can expect no second-harmonic Hall current in these structures. However, as shown in the right panel of Fig. 5b, the

CW-twisted 4-layer exhibits a significant response comparable to the CC-twisted bilayer with a 2Ω Berry curvature. Since this response is unexpected based on the traditional understanding, we designate this as an **"unconventional nonlinear Hall effect."**

III. DISCUSSION

To understand and classify the unconventional Hall response observed in the CW-twisted 4-layer structure (Fig. 5b), we extend our analysis to various stacking orders of 4-layers. As seen in Fig. 6a, we start from the (A, B', B, A') structure with Berry curvatures of $(\Omega, \Omega, -\Omega, -\Omega)$. In this case, the total Berry curvature and the current density response are zero. When we do a cyclic permutation by bringing the top layer under the bottom one (as seen in Fig. 6b), the stacking and corresponding Berry curvature become (A', A, B', B) and $(-\Omega, \Omega, \Omega, -\Omega)$, respectively. Even though the total Berry curvature is still zero and the same layers are used, the system now has a non-zero real-time response after a slight change in the layer ordering.

Next, we test the stacking order obtained by switching the 2nd and 3rd layers of the last structure (see Fig. 6c). The stacking is now (A', B', A, B), and the corresponding Berry curvatures are not affected by this transformation as the inner two layers have the same Berry curvature: $(-\Omega, \Omega, \Omega, -\Omega)$. By flipping the layers, we break the twistedness of the structure, which cannot be formed by a directional torsion force, but keep the ordering of Berry curvatures. The resultant real-time response is the same as the previous structure. Thus, we conclude that the unconventional Hall effect occurs regardless of special geometric ordering. Instead, the observed phenomenon appears to be related to the order of the Berry curvatures of the layers.

Lastly, we flip the 1st and 2nd layer of the previous structure and obtain the stacking (B', A', A, B) with the Berry curvature ordering $(\Omega, -\Omega, \Omega, -\Omega)$ (see Fig. 6d). Now, the Berry curvature order has been changed, and the system shows no real-time response.

The 4-layer structures with the Berry curvature ordering of $(\Omega, \Omega, -\Omega, -\Omega)$ and $(\Omega, -\Omega, \Omega, -\Omega)$ have no response that is consistent with the total Berry curvature. When the layers are ordered in such a way that their Berry curvatures are $(-\Omega, \Omega, \Omega, -\Omega)$, we observe an unconventional nonlinear Hall effect. The common property of the former two structures is that they have an odd-symmetry Berry curvature (with respect to the center of the system) in the *z*-direction. However, the latter ordering has an even symmetry in the *z*-direction. The system must be non-centrosymmetric to observe the Hall effect as the Berry curvature vanishes in the presence of an inversion center. Even though all our twisted 4-layers are non-centrosymmetric and have zero Berry curvature, the presence of odd-ordered Berry curvature is a secondary requirement to suppress the Hall effect. On the other hand, the presence of an even-ordered Berry curvature allows an unexpected Hall effect. If the layers were completely non-interacting, then each layer's nonlinear transverse current response would independently obey its own Berry curvature, and the total response would be zero for any system in Fig. 6. Consequently, the interlayer interactions have some crucial role in the observation of these non-zero responses.

To explore the role of the interlayer interactions in second-harmonic Hall responses, we carried out RT-TDDFT calculations for BBAA and BAAB 4-layers with various separations whose Berry curvatures are $(-\Omega, -\Omega, \Omega, \Omega)$ and $(-\Omega, \Omega, \Omega, -\Omega)$, respectively (see Figs. 7a and 7d). When the interlayer separation distance is set to $d = 10$ Å, the layers are non-interacting, and as seen in Figs. 7b and 7e, produce negligible responses. However, when the layers are separated by the geometry-optimized distance of $d = 3.5$ Å, a nonlinear Hall response is obtained for BAAB stacking. The responses shown in Figs. 7c and 7f are similar to Figs. 6a and 6b, which have different stacking but the same Berry curvature ordering with the BBAA and BAAB stackings, respectively. This result proves that the origin of the unconventional Hall effect observed in Figs. 5b, 6b, 6c, and 7f is the interlayer interaction, and the effect disappears when the layers are not interacting.

To further analyze the interlayer interactions, we constructed 8×8 model Hamiltonians that mimic BBAA and BAAB stackings (see Figs. 8a and 8g). For simplicity, we consider only A and B layers with two basis atoms per layer in the unit cell instead of twisted layers with fourteen basis atoms in the $\sqrt{7}\times\sqrt{7}$ supercell. Even though the BBAA stacking is centrosymmetric and is expected to not exhibit the Hall effect, it is used here as a representative system with odd-ordered Berry curvature. We adopt the BAAB stacking to reveal the role of interlayer interactions in the unconventional Hall effect in structures with an even-ordered Berry curvature.

The minimal model Hamiltonian in momentum space for the 4-layer structures can be constructed as follows:

$$\widehat{H}(\mathbf{k}) = \begin{bmatrix} m_1 & f & T_{12} & T_{12} & & & & \\ f^* & -m_1 & 0 & f & T_{23} & T_{23} & & \\ T_{12} & 0 & m_2 & f^* & -m_2 & 0 & T_{34} & T_{34} \\ & T_{12} & f^* & -m_2 & 0 & m_3 & f & 0 \\ & & T_{23} & 0 & m_3 & f^* & -m_3 & 0 \\ & & & T_{23} & f^* & -m_3 & 0 & m_4 \\ & & & & T_{34} & 0 & m_4 & f \\ & & & & & T_{34} & f^* & -m_4 \end{bmatrix}, \tag{9}$$

where m_i is the mass term originating from the on-site energy difference between boron and nitrogen basis atoms at the ith layer, which is set to $m_i = m = 2.73$ eV if the ith layer has a B configuration, and $m_i = -m$ if it has an A configuration. The $f = t_{\mathrm{H}}\left(e^{i\mathbf{k}\cdot\boldsymbol{\tau}_1} + e^{i\mathbf{k}\cdot\boldsymbol{\tau}_2} + e^{i\mathbf{k}\cdot\boldsymbol{\tau}_3}\right)$ term models the intralayer hopping between nearest-neighbor atoms, where $t_{\mathrm{H}} = 2.00$ eV is the intralayer hopping integral, and $\boldsymbol{\tau}_i$ are the vectors connecting a chosen atom with its three neighboring atoms in the same layer in the hexagonal unit cell. As shown above, $T_{i,i+1} = T_{\mathrm{H}}e^{i\mathbf{k}\cdot\mathbf{c}}$ is the interlayer hopping between nearest-neighbor atoms in the ith and (i+1)th layer, where $T_{\mathrm{H}} = 1.00$ eV is the interlayer hopping integral, and $\mathbf{c}$ is a vector in the z-direction connecting a chosen atom with its vertical neighbor in the upper layer. Here, we assume only a nearest-neighbor interaction, and thus, the hopping occurs between the same (different) type of atoms for AA and BB (AB and BA) stacked neighboring layers. The

magnitude of T_H is inversely proportional to the interlayer distance d such that larger interlayer distances correspond to smaller interlayer hopping strengths (and vice versa). Similar to Eq. (6), we solve the time-dependent model Hamiltonian equation given by $i\hbar\frac{\partial}{\partial t}|\psi_{n\mathbf{k}}(t)\rangle = \hat{H}\left(\mathbf{k}-\frac{e}{c}\mathbf{A}(t)\right)|\psi_{n\mathbf{k}}(t)\rangle$ with the same field described in Eq. (7).

When the interlayer hopping interaction is not included, there is no transverse response regardless of stacking order, as seen in Figs. 8b and 8h. However, only BAAB stacking has a finite response when the interlayer interactions are turned on (see Figs. 8c and 8i), as observed in our RT-TDDFT calculations in Figs. 7c and 7f. To fully understand this effect, we analyze pairwise interlayer interactions. The interlayer distance is approximately 3.5 Å, and next-nearest layer interactions can be safely neglected. Thus, we can examine the nearest-neighbor layer pairs by adjusting the parameters T_{12}, T_{23}, and T_{34}.

As shown in Figs. 5b and 5c, bilayers with the same Berry curvatures exhibit a Hall response, while those with opposite Berry curvatures do not. Taking this into account, we can turn on the hopping between the BB layer pair in the BBAA stacking ($T_{12} > 0$, $T_{23} = T_{34} = 0$) and obtain a non-zero response (see Fig. 8d) as expected from Fig. 5c. This response solely originates from the interlayer coupling of the 1st and 2nd layers since the summation of the individual layers' responses is zero as shown in Fig. 8c. Next, we can turn on the hopping between the BA layer pair only ($T_{23} > 0$, $T_{12} = T_{34} = 0$) and observe a zero response (see Fig. 8e) as expected from Fig. 5b. Lastly, when the hopping is allowed between only the AA layer pair ($T_{34} > 0$, $T_{12} = T_{23} = 0$) (see Fig. 8f), we obtain the exact opposite response of the case with hopping between only the BB layer pair. This is a reasonable result since the B and A layers have opposite Berry curvatures, and these individual responses can be considered as contributions of each layer pair to the total response of the entire interacting system. Thus, the contributions from the BB pair and AA pair cancel each other. Since the BA pair has no

contribution, the resultant total response becomes zero, as obtained in Fig. 8c. We repeat the same analysis for the BAAB stacking and obtain zero response when the BA or AB layer pairs are interacting (see Figs. 8j and 8l, which are same as Fig. 8e). In comparison, a finite response is obtained when the AA layer pair is coupled (see Fig. 8k, which is the same as Fig. 8f). Since there is no other pair that can cancel the contribution of the AA pair, the fully-interacting BAAB structure also has a finite transverse response, which we previously designated as an unconventional nonlinear Hall effect. The same pairwise analysis can explain the responses obtained in Figs. 5 and 6 for the bi-, 3-, and 4-layer structures.

Our model Hamiltonian analysis in Fig. 8 shows that the unconventional Hall response originates from interlayer hopping between neighboring layers with the same Berry curvatures. Specifically, when two layers with opposite Berry curvatures interact, the electrons tend to move in opposite transverse directions, and upon hopping, they encounter an opposing current contribution, which cancels out any net transverse current. In contrast, when layers with the same Berry curvature interact, the electrons move in the same transverse direction, and upon hopping, they contribute to the same current direction, generating a net transverse current. This cooperative interaction explains why only layers with aligned Berry curvatures contribute to the unconventional Hall response. Additionally, we assume that the dominant interactions are between nearest-neighbor layers, effectively treating them as bilayers, while next-nearest-neighbor interactions are negligible. In conclusion, the Hall response in the system arises from both the additive Berry curvatures of individual layers and the enhanced contribution from interacting bilayer pairs with aligned Berry curvatures, which together produce the observed responses in the multilayer systems.

The semi-classical approach explained above can be attributed to the higher-order contributions of the interband Berry curvature between bands of nearest-neighbor layers. However, our results indicate that those contributions do not originate from Berry curvature

multipoles as they are proportional to the Berry curvature [39]. One of us previously defined a three-band term that contributes to this response but did not show any physical connection between this term and the Berry curvature [11]. Our findings in this work now provide a qualitative mechanistic relationship between the three-band term and Berry curvature through these interlayer interactions.

We extended our analysis to 6-layer systems to understand the role of interlayer interactions in the unconventional Hall effect (see Fig. 9). Similar to the 4-layer systems, we obtain finite contributions from neighboring layers with the same Berry curvatures (Figs. 9d, 9f, and 9l), whereas the interaction between layers with opposite Berry curvatures does not generate a transverse response (Figs. 9c, 9e, 9i, 9j, and 9k). Also, the AA and BB pairs induce responses in opposite directions (Figs. 9d and 9f). Thus, the ABBAAB stacking has no net response (Fig. 9b), whereas ABABBA stacking exhibits a net Hall current due to the BB layer pair (Fig. 9h).

We analyze twisted bulk structures for possible Hall effects to extend our scope beyond the finite multilayer slabs. In Figs. 10a and 10b, we construct two bulk systems with unit cells with AB'BA' and A'AB'B stacking, respectively. The 4-layer slabs of the same stackings were discussed in Figs. 6a and 6b, which concluded that the A'AB'B stacked 4-layer with Berry curvature order $(-\Omega, \Omega, \Omega, -\Omega)$ exhibits a Hall current due to the non-zero summation of pairwise interlayer interactions of nearest-neighbor layers, whereas the AB'BA' stacked 4-layer with $(\Omega, \Omega, -\Omega, -\Omega)$ does not, as it has odd-ordered Berry curvatures in the *z*-direction. However, the bulk systems are periodic in the *z*-direction, and the periodic image of the 1st layer is the nearest neighbor of the 4th layer. Therefore, we need to include the contribution of the interlayer interaction between the 4th and 1st layers, which are the BA' layer pair with $(-\Omega, -\Omega)$ for the A'AB'B stacking and the A'A layer pair with $(-\Omega, \Omega)$ for the AB'BA' stacking. Adding the $(-\Omega, -\Omega)$ pair brings an opposite contribution to the (Ω, Ω) pair located in the middle of the A'AB'B stacking. This interaction eliminates the Hall effect, as

seen in the transformation from Fig. 6b to Fig. 10b. Conversely, adding the $(-\Omega, \Omega)$ pair has no contribution to the AB'BA' stacking as obtained from Figs. 5b, 8e, 8j, and 8l. This result can also be observed by comparing Figs. 6a and 10a. As a result, the bulk structures of both stackings have no Hall effect due to interlayer interaction of periodic layers.

The lack of an unconventional Hall effect in bulk structures can also be attributed to the symmetry of the Berry curvatures of the layers. As seen in Figs. 6a and 10a, the ordering $(\Omega, \Omega, -\Omega, -\Omega)$ of both 4-layer and bulk structures are odd with respect to the plane in the middle of the 2nd and 3rd layers (the dashed red line in Fig. 10a). However, the ordering $(-\Omega, \Omega, \Omega, -\Omega)$ is even for a 4-layer A'AB'B stacking (see Fig. 6b). In contrast, its bulk counterpart is also odd with respect to the plane in the middle of 3rd and 4th layers of the periodic unit cell (the dashed red line in Fig. 10b). This can be seen more easily when we explicitly examine the ordering of 2 consecutive unit cells $\cdots(-\Omega, \Omega, \Omega, -\Omega)(-\Omega, \Omega, \Omega, -\Omega)(-\Omega, \cdots$, which is identical to the ordering $\cdots -\Omega)(\Omega, \Omega, -\Omega, -\Omega)(\Omega, \Omega, -\Omega, -\Omega)\cdots$. The AB'BA' and A'AB'B stackings are identical in the periodic bulk structures, emphasizing the role of Berry curvature ordering on the unconventional Hall effect in finite multilayers.

In this study, we have demonstrated novel nonlinear Hall effects in insulating multilayer materials, focusing on hexagonal boron nitride (h-BN) as an example. We surprisingly find that the effect is governed not only by the cumulative Berry curvature dipoles of individual layers, as traditionally anticipated, but by the interlayer interactions mediated by Berry curvatures of neighboring layers. Unlike conventional material systems, our analysis reveals a distinct second-harmonic transverse response in twisted h-BN four-layers, where the overall Berry curvature sum is nullified.

Through rigorous large-scale RT-TDDFT calculations and analytical modeling of various

four-layer configurations, we demonstrate that the nonlinear Hall effect in stacked h-BN multilayers is critically influenced by the stacking order and pairwise interactions of the layers. This insight extends beyond four-layer systems, providing a framework to interpret phenomena observed in bilayer, three-layer structures, and bulk materials. Furthermore, we simplify the prediction of nonlinear responses by conducting symmetry analysis on Berry curvatures of stacked layers.

Our results highlight the distinct nonlinear optical behavior enabled by oppositely twisted stacking configurations that can be modulated by applying directional torsion forces to h-BN multilayers. Moreover, these unexpected findings advance our understanding of nonlinear optical response mechanisms and open new avenues for designing innovative multilayer materials with controllable optoelectronic applications that can be modulated by mechanical deformation.

METHODS

The ground-state electronic structures, Berry curvatures, and real-time electron dynamics were obtained using a custom version of the Qbox package [37, 38, 49, 50] developed by our group. We used the Perdew–Burke–Ernzerhof (PBE) generalized gradient approximation functional [51] with scalar-relativistic norm-conserving pseudopotentials to describe the atomic potentials [52]. The planewave cutoff energy and energy convergence threshold were set to 1088 and 2.7×10^{-11} eV, respectively. The $\sqrt{7} \times \sqrt{7}$supercells (primitive cell for only Figs. 7b and 7i) with a vacuum slab of 10 Å were used to calculate h-BN monolayer and multilayer slabs. We obtained an interlayer distance of ~3.5 Å via geometry optimization with the SCAN functional using a force threshold of 0.01 eV/Å [53]. The Brillouin zone integration was carried out using a Gamma-centered 9×9×1 mesh for time-dependent calculations, excluding any symmetry operation, and a non-irreducible 12×12×1 mesh with an additional 120 k-point

across the M-K-Γ-K'-M path for the Berry curvature calculations. The plane waves and k-points were parallelized on 5 and 81 CPU ranks, respectively, for the time-dependent calculations, while the G- and k-points were parallelized on 6 and 20 CPU ranks, respectively, for the Berry curvature calculations. For the time propagation computations, we used a Crank-Nicolson time propagation scheme [54] with a time interval and energy convergence set to 1.2 as and 2.7×10^{-8} eV, respectively. To minimize the propagation noise in our current density calculations, we subtracted the zero-perturbation response, J_0, which we obtained from the time propagation of the system without an applied driving field, from all our calculated real-time responses. To obtain a pure second harmonic response, $J^{2\omega}$, we added the responses to applied laser fields with opposite signs, J_{+E} and J_{-E}, resulting in a second harmonic current of the form $J^{2\omega} = (J_{+E} + J_{-E})/2 - J_0$.

Data availability

The calculated numerical data in this study are available from the corresponding author upon reasonable request.

Code availability

The Fortran and RT-TDDFT codes used to perform the calculations in this study are available from the corresponding author upon reasonable request.

Acknowledgements

This work was supported by the U.S. Department of Energy, Office of Science, Office of Advanced Scientific Computing Research, Scientific Discovery through the Advanced Computing (SciDAC) program under Award Number DE-SC0022209. This research used resources of the National Energy Research Scientific Computing Center (NERSC), a U.S. Department of Energy Office of Science User Facility located at Lawrence Berkeley National

Laboratory, operated under Contract No. DE-AC02-05CH11231 using NERSC award BES-ERCAP0023692.

Author contributions

M.S.O. performed the *ab initio* calculations, developed the model Hamiltonian code, and analyzed the data; M.S.O., M.C., Q.X., and B.M.W. wrote the manuscript. M.S.O., M.C., Q.X., A.P.D., M.D.B., K.Z.I., and B.M.W. have read and approved the manuscript.

Competing interests

The authors declare that they have no competing interests.

References

[1] J. Orenstein, J. E. Moore, T. Morimoto, D. H. Torchinsky, J. W. Harter, and D. Hsieh. Topology and Symmetry of Quantum Materials via Nonlinear Optical Responses. *Annual Review of Condensed Matter Physics, Vol 12, 2021*, **12**, 247-272, 2021.

[2] J. W. You, S. R. Bongu, Q. Bao, and N. C. Panoiu. Nonlinear optical properties and applications of 2D materials: theoretical and experimental aspects. *Nanophotonics*, **8**, 63-97, 2019.

[3] L. L. Zhou, H. G. Fu, T. Lv, C. B. Wang, H. Gao, D. Q. Li, L. M. Deng, and W. Xiong. Nonlinear Optical Characterization of 2D Materials. *Nanomaterials*, **10**, 2020.

[4] A. Taghizadeh, K. S. Thygesen, and T. G. Pedersen. Two-Dimensional Materials with Giant Optical Nonlinearities near the Theoretical Upper Limit. *Acs Nano*, **15**, 7155-7167, 2021.

[5] S. Dengler and B. Eberle. Investigations on the Nonlinear Optical Properties of 0D, 1D, and 2D Boron Nitride Nanomaterials in the Visible Spectral Region. *Nanomaterials*, **13**, 2023.

[6] J. S. Ginsberg, M. M. Jadidi, J. Zhang, C. Y. Chen, N. Tancogne-Dejean, S. H. Chae, G. N. Patwardhan, L. Xian, K. Watanabe, T. Taniguchi, J. Hone, A. Rubio, and A. L. Gaeta. Phonon-enhanced nonlinearities in hexagonal boron nitride. *Nature Communications*, **14**, 2023.

[7] F. Iyikanat, A. Konecná, and F. J. G. de Abajo. Nonlinear Tunable Vibrational Response in Hexagonal Boron Nitride. *Acs Nano*, **15**, 13415-13426, 2021.

[8] G. J. Lee, K. M. Jyothsna, J. Park, J. Lee, V. Raghunathan, and H. Kim. Confocal nonlinear optical imaging on hexagonal boron nitride nanosheets. *Photonix*, **4**, 2023.

[9] S. Kim, J. E. Fröch, A. Gardner, C. Li, I. Aharonovich, and A. S. Solntsev. Second-harmonic generation in multilayer hexagonal boron nitride flakes. *Optics Letters*, **44**, 5792-5795, 2019.

[10] I. Sodemann and L. Fu. Quantum Nonlinear Hall Effect Induced by Berry Curvature Dipole in Time-Reversal Invariant Materials. *Physical Review Letters*, **115**, 2015.
[11] M. S. Okyay, S. A. Sato, K. W. Kim, B. H. Yan, H. Jin, and N. Park. Second harmonic Hall responses of insulators as a probe of Berry curvature dipole. *Communications Physics*, **5**, 2022.
[12] Z. Z. Du, C. M. Wang, H. P. Sun, H. Z. Lu, and X. C. Xie. Quantum theory of the nonlinear Hall effect. *Nature Communications*, **12**, 2021.
[13] Z. Z. Du, H. Z. Lu, and X. C. Xie. Nonlinear Hall effects. *Nature Reviews Physics*, **3**, 744-752, 2021.
[14] C. Ortix. Nonlinear Hall Effect with Time-Reversal Symmetry: Theory and Material Realizations. *Advanced Quantum Technologies*, **4**, 2021.
[15] A. Tiwari, F. C. Chen, S. Z. Zhong, E. Drueke, J. Koo, A. Kaczmarek, C. Xiao, J. J. Gao, X. Luo, Q. Niu, Y. P. Sun, B. H. Yan, L. Y. Zhao, and A. W. Tsen. Giant c-axis nonlinear anomalous Hall effect in Td-MoTe2 and WTe2. *Nature Communications*, **12**, 2021.
[16] M. Z. Huang, Z. F. Wu, J. X. Hu, X. B. Cai, E. Li, L. H. An, X. M. Feng, Z. Q. Ye, N. Lin, K. T. Law, and N. Wang. Giant nonlinear Hall effect in twisted bilayer WSe2. *National Science Review*, **10**, 2023.
[17] Q. Ma, S. Y. Xu, H. T. Shen, D. MacNeill, V. Fatemi, T. R. Chang, A. M. M. Valdivia, S. F. Wu, Z. Z. Du, C. H. Hsu, S. Fang, Q. D. Gibson, K. Watanabe, T. Taniguchi, R. J. Cava, E. Kaxiras, H. Z. Lu, H. Lin, L. Fu, N. Gedik, and P. Jarillo-Herrero. Observation of the nonlinear Hall effect under time-reversal-symmetric conditions. *Nature*, **565**, 337-+, 2019.
[18] T. Ma, H. Chen, K. Yananose, X. Zhou, L. Wang, R. L. Li, Z. Y. Zhu, Z. Y. Wu, Q. H. Xu, J. J. Yu, C. W. Qiu, A. Stroppa, and K. P. Loh. Growth of bilayer MoTe2
single crystals with strong nonlinear Hall effect. *Nature Communications*, **13**, 2022.
[19] K. F. Kang, T. X. Li, E. Sohn, J. Shan, and K. F. Mak. Nonlinear anomalous Hall effect in few-layer WTe. *Nature Materials*, **18**, 324-+, 2019.
[20] H. Wang and X. F. Qian. Ferroelectric nonlinear anomalous Hall effect in few-layer WTe. *Npj Computational Materials*, **5**, 2019.
[21] R. Habara and K. Wakabayashi. Nonlinear optical Hall effect of few-layered NbSe2. *Physical Review Research*, **4**, 2022.
[22] L. Ma, Y. Li, H. R. Fu, N. Tian, and C. Y. You. Topological Hall effect in Pd/CoZr/MgO multilayer films. *Applied Physics Letters*, **121**, 2022.
[23] H. Li, M. X. Li, R. C. Xiao, W. H. Liu, L. Wu, W. Gan, H. Han, X. Tang, C. J. Zhang, and J. N. Wang. Current induced second-order nonlinear Hall effect in bulk WTe. *Applied Physics Letters*, **123**, 2023.
[24] T. N. Ikeda. High-order nonlinear optical response of a twisted bilayer graphene. *Physical Review Research*, **2**, 2020.
[25] L. D. Xian, D. M. Kennes, N. Tancogne-Dejean, M. Altarelli, and A. Rubio. Multiflat Bands and Strong Correlations in Twisted Bilayer Boron Nitride: Doping-Induced Correlated

Insulator and Superconductor. *Nano Letters*, **19**, 4934-4940, 2019.
[26] J. P. Liu and X. Dai. Anomalous Hall effect, magneto-optical properties, and nonlinear optical properties of twisted graphene systems. *Npj Computational Materials*, **6**, 2020.
[27] G. Demetriou, H. T. Bookey, F. Biancalana, E. Abraham, Y. Wang, W. Ji, and A. K. Kar. Nonlinear optical properties of multilayer graphene in the infrared. *Optics Express*, **24**, 13033-13043, 2016.
[28] B. Can-Uc, J. López, E. G. Lizarraga-Medina, H. A. Borbon-Nuñez, R. Rangel-Rojo, H. Marquez, H. Tiznado, J. A. Jurado-González, and G. Hirata-Flores. Third-order nonlinear optical properties of a multilayer Al2O3/ZnO for nonlinear optical waveguides. *Optics Express*, **27**, 17359-17368, 2019.
[29] G. Sachdeva, S. Kaur, R. Pandey, and S. P. Karna. First-Principles Study of Linear and Nonlinear Optical Properties of Multi-Layered Borophene. *Computation*, **9**, 2021.
[30] Y. Cao, V. Fatemi, S. Fang, K. Watanabe, T. Taniguchi, E. Kaxiras, and P. Jarillo-Herrero. Unconventional superconductivity in magic-angle graphene superlattices. *Nature*, **556**, 43-+, 2018.
[31] V. Pandey, S. Mishra, N. Maity, S. Paul, M. B. Abhijith, A. K. Roy, N. R. Glavin, K. Watanabe, T. Taniguchi, A. K. Singh, and V. Kochat. Probing Interlayer Interactions and Commensurate-Incommensurate Transition in Twisted Bilayer Graphene through Raman Spectroscopy. *Acs Nano*, **18**, 4756-4764, 2024.
[32] S. M. Shinde, K. P. Dhakal, X. Chen, W. S. Yun, J. Lee, H. Kim, and J. H. Ahn. Stacking-controllable interlayer coupling and symmetric configuration of multilayered MoS. *Npg Asia Materials*, **10**, 2018.
[33] Z. J. Wang, J. C. Dong, Y. Cui, G. Eres, O. Timpe, Q. Fu, F. Ding, R. Schloegl, and M. G. Willinger. Stacking sequence and interlayer coupling in few-layer graphene revealed by in situ imaging. *Nature Communications*, **7**, 2016.
[34] E. Runge and E. K. U. Gross. Density-Functional Theory for Time-Dependent Systems. *Physical Review Letters*, **52**, 997-1000, 1984.
[35] K. Burke, J. Werschnik, and E. K. U. Gross. Time-dependent density functional theory: Past, present, and future. *Journal of Chemical Physics*, **123**, 2005.
[36] D. Shin, G. Lee, Y. Miyamoto, and N. Park. Real-Time Propagation via Time-Dependent Density Functional Theory Plus the Hubbard U Potential for Electron-Atom Coupled Dynamics Involving Charge Transfer. *Journal of Chemical Theory and Computation*, **12**, 201-208, 2016.
[37] F. Gygi. Architecture of Qbox: A scalable first-principles molecular dynamics code. *Ibm Journal of Research and Development*, **52**, 137-144, 2008.
[38] F. Gygi, R. K. Yates, J. Lorenz, E. W. Draeger, F. Franchetti, C. W. Ueberhuber, B. R. d. Supinski, S. Kral, J. A. Gunnels, and J. C. Sexton. Large-Scale First-Principles Molecular Dynamics simulations on the BlueGene/L Platform using the Qbox code. In *SC '05:*

Proceedings of the 2005 ACM/IEEE Conference on Supercomputing, 2005, pp. 24-24.
[39] C. P. Zhang, X. J. Gao, Y. M. Xie, H. C. Po, and K. T. Law. Higher-order nonlinear anomalous Hall effects induced by Berry curvature multipoles. *Physical Review B*, **107**, 2023.
[40] M. Feuerbacher. Moire, Euler and self-similarity - the lattice parameters of twisted hexagonal crystals. *Acta Crystallographica a-Foundation and Advances*, **77**, 460-471, 2021.
[41] P. K. Nayak, Y. Horbatenko, S. Ahn, G. Kim, J. U. Lee, K. Y. Ma, A. R. Jang, H. Lim, D. Kim, S. Ryu, H. Cheong, N. Park, and H. S. Shin. Probing Evolution of Twist-Angle-Dependent Interlayer Excitons in MoSe2/WSe2 van der Waals Heterostructures. *Acs Nano*, **11**, 4041-4050, 2017.
[42] S. H. Kazemi and M. Mahmoudi. Chirality-dependent optical dipole potential. *Physica Scripta*, **95**, 2020.
[43] D. Y. Fu, J. L. Xin, Y. Y. He, S. C. Wu, X. Y. Zhang, X. M. Zhang, and J. H. Luo. Chirality-Dependent Second-Order Nonlinear Optical Effect in 1D Organic-Inorganic Hybrid Perovskite Bulk Single Crystal. *Angewandte Chemie-International Edition*, **60**, 20021-20026, 2021.
[44] S. Imaki and A. Yamamoto. Lattice field theory with torsion. *Physical Review D*, **100**, 2019.
[45] R. Soto-Garrido, E. Muñoz, and V. Juricic. Dislocation defect as a bulk probe of monopole charge of multi-Weyl semimetals. *Physical Review Research*, **2**, 2020.
[46] D. B. Shin, S. A. Sato, H. Hübener, U. De Giovannini, J. Kim, N. Park, and A. Rubio. Unraveling materials Berry curvature and Chern numbers from real-time evolution of Bloch states. *Proceedings of the National Academy of Sciences of the United States of America*, **116**, 4135-4140, 2019.
[47] R. Naaman and D. H. Waldeck. Chiral-Induced Spin Selectivity Effect. *Journal of Physical Chemistry Letters*, **3**, 2178-2187, 2012.
[48] B. P. Bloom, Y. Paltiel, R. Naaman, and D. H. Waldeck. Chiral Induced Spin Selectivity. *Chemical Reviews*, **124**, 1950-1991, 2024.
[49] F. Gygi, I. Duchemin, D. Donadio, and G. Galli. Practical algorithms to facilitate large-scale first-principles molecular dynamics. *Scidac 2009: Scientific Discovery through Advanced Computing*, **180**, 2009.
[50] F. Gygi, E. W. Draeger, M. Schulz, B. R. d. Supinski, J. A. Gunnels, V. Austel, J. C. Sexton, F. Franchetti, S. Kral, C. W. Ueberhuber, and J. Lorenz, in *Proceedings of the 2006 ACM/IEEE conference on Supercomputing* (Association for Computing Machinery, Tampa, Florida, 2006), pp. 45–es.
[51] J. P. Perdew, K. Burke, and M. Ernzerhof. Generalized gradient approximation made simple. *Physical Review Letters*, **77**, 3865, 1996.
[52] D. R. Hamann. Optimized norm-conserving Vanderbilt pseudopotentials. *Physical Review B*, **88**, 2013.
[53] J. W. Sun, A. Ruzsinszky, and J. P. Perdew. Strongly Constrained and Appropriately

Normed Semilocal Density Functional. *Physical Review Letters*, **115**, 2015.
[54] J. Crank and P. Nicolson. A practical method for numerical evaluation of solutions of partial differential equations of the heat-conduction type. *Advances in Computational Mathematics*, **6**, 207-226, 1996.

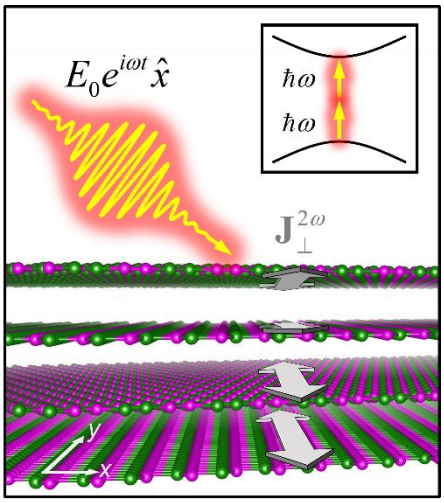

Figure 1. Illustration of transverse second-harmonic generation in a twisted h-BN multilayer. The yellow arrows in the figure and the inset represent the applied laser pulse polarized in the *x*-direction. The pulse frequency ω is slightly larger than half the bandgap. The gray arrows on the h-BN layers depict the transverse second-harmonic generation in the *y*-direction.

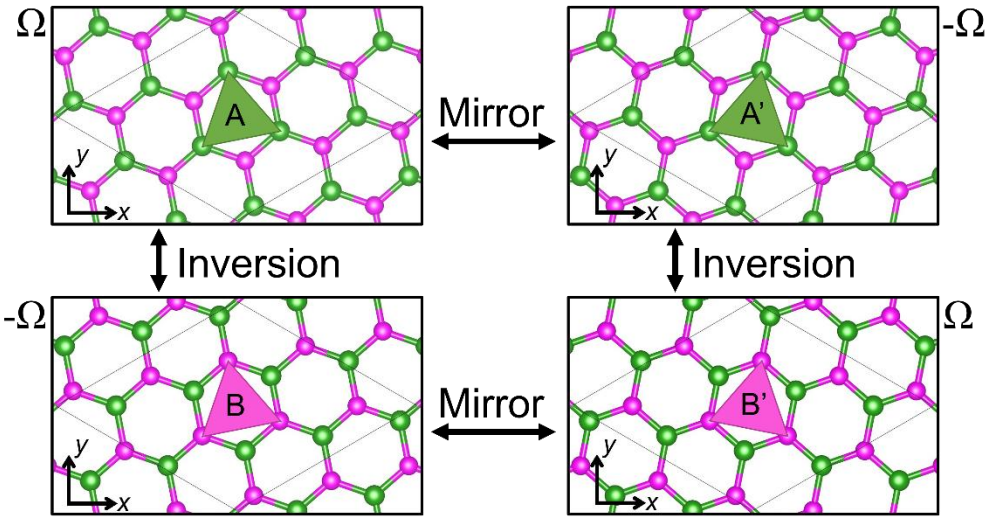

Figure 2. Possible configurations of h-BN on a $\sqrt{7} \times \sqrt{7}$ supercell. We label four possible configurations as A, A', B, and B'. These configurations are connected with mirror and inversion symmetries: A-A' and B-B' are mirror pairs, and A-B and A'-B' are inversion pairs. Accordingly, the Berry curvature of each configuration has an opposite sign with a symmetry pair.

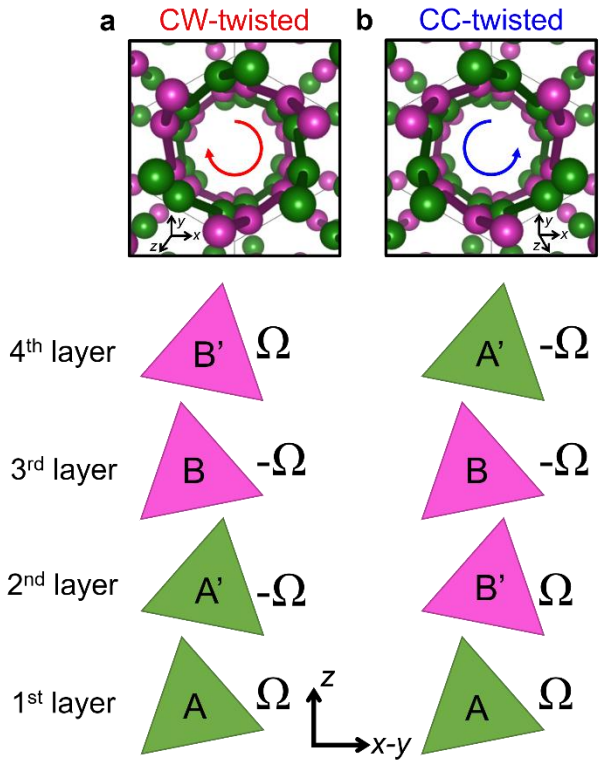

Figure 3. Construction of a twisted h-BN 4-layer. The upper panels of **a** and **b** are top views of clockwise- and counterclockwise-twisted (abbreviated as CW- and CC-twisted) h-BN multilayers, respectively. The lower panels show the corresponding out-of-plane layer ordering up to the fourth layer and the Berry curvature of each layer in the twisted multilayers.

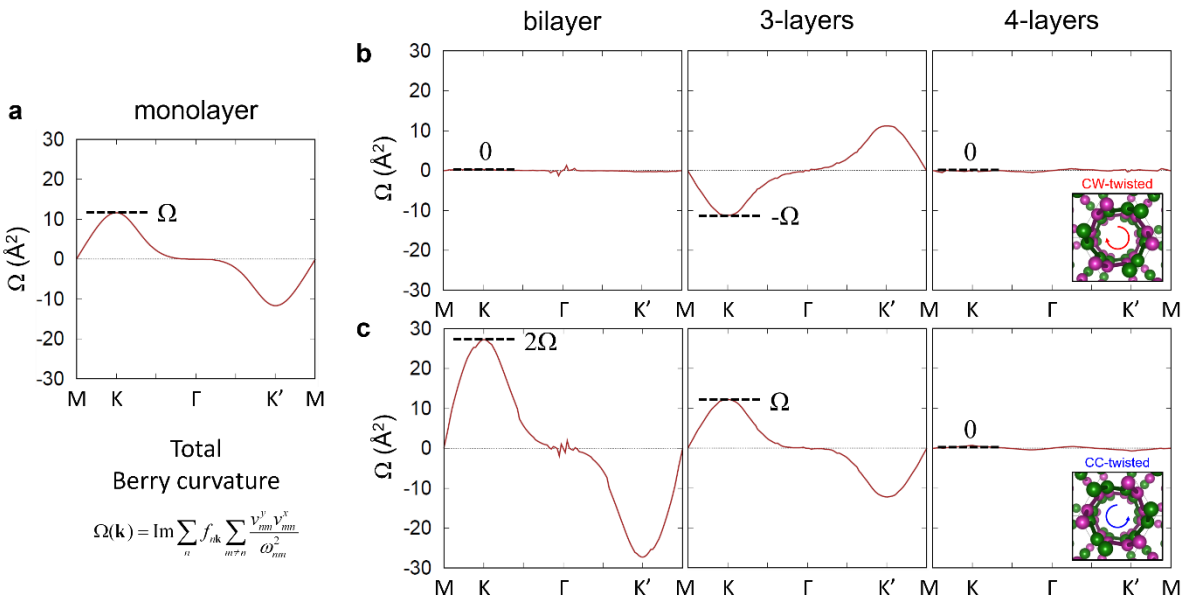

Figure 4. Momentum-resolved Berry curvatures of twisted h-BN multilayers. The total Berry curvature of a h-BN monolayer as a function of momentum vector, **k**, is shown in panel **a**. The monolayer is constructed on a $\sqrt{7} \times \sqrt{7}$ supercell with configuration A. The left, middle, and right sub-plots in panel **b** are total Berry curvatures of the left-handed bilayer (AA'), 3-layers (AA'B), and 4-layers (AA'BB'), respectively. Panel **c** is the same for the right-handed bilayer (AB'), 3-layers (AB'B), and 4-layers (AB'BA'), respectively. The insets in the right panels of **b** and **c** are the top views of left- and right-handed multilayers, respectively.

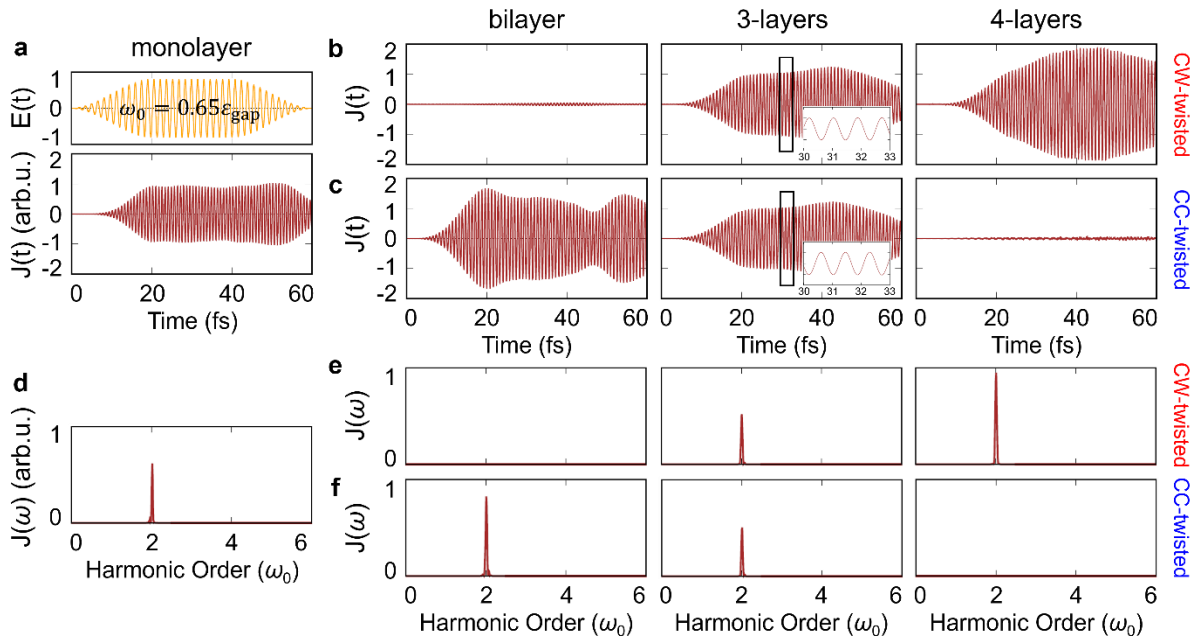

Figure 5. Real-time transverse second-harmonic optical responses of twisted h-BN multilayers. The upper and lower sub-plots in panel **a** are the real-time profiles of the applied laser field current density response, respectively, of the h-BN monolayer. The left, middle, and right sub-plots in panel **b** are the current density responses of the left-handed bilayer (AA'), 3-layers (AA'B), and 4-layers (AA'BB'), respectively. Panel **c** is the same for the right-handed bilayer (AB'), 3-layers (AB'B), and 4-layers (AB'BA'), respectively. The same units are used for all current responses. Panels **d**, **e**, and **f** are Fourier transforms of the monolayer, CW-twisted multilayers, and CC-twisted multilayers, respectively.

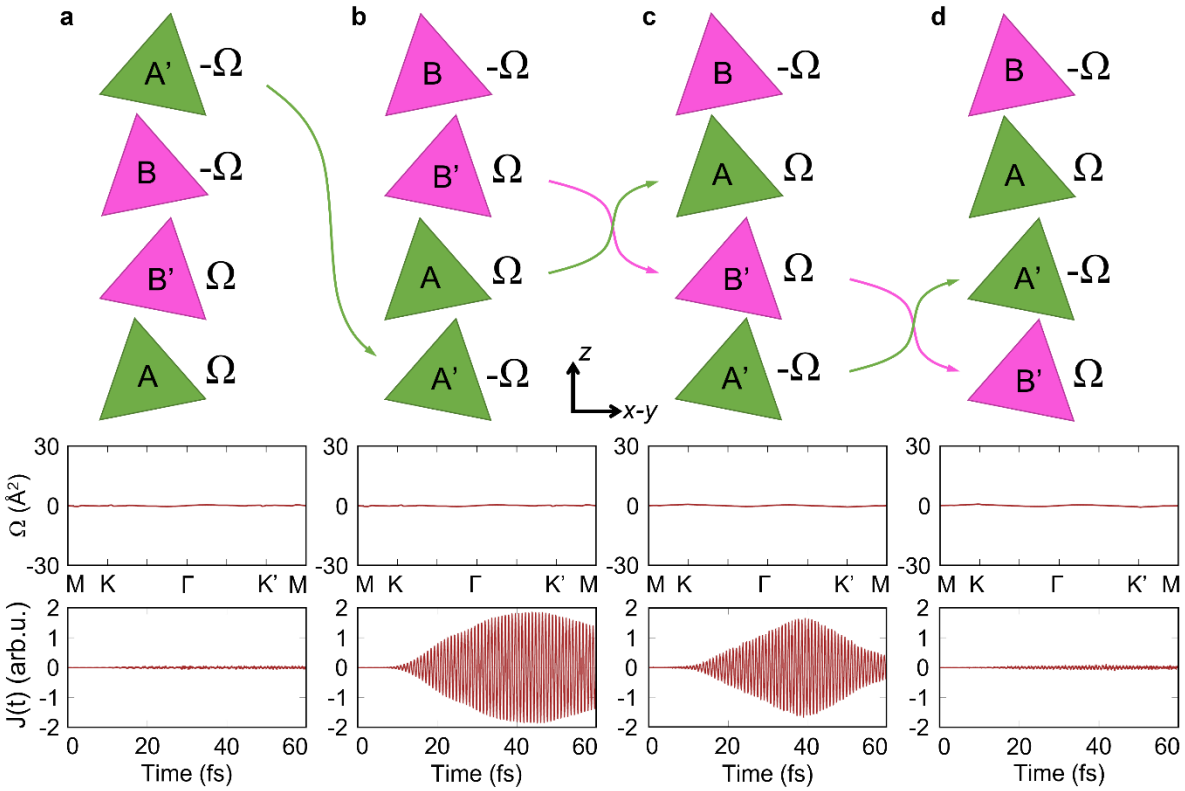

Figure 6. Berry curvature and current responses of various orderings of a h-BN 4-layer. The upper panels illustrate the out-of-plane layer orderings for various 4-layer structures. The middle and lower panels are the momentum-resolved Berry curvatures and the real-time current density responses of the corresponding structures, respectively. Panel **a** shows AB'BA stacking, which is also shown in Figs. 3c and 4c. Configuration **b** is obtained by placing the top A' layer of panel **a** on the bottom. Configuration **c** (**d**) is obtained by interchanging the middle (bottom) two layers of configuration **b** (**c**).

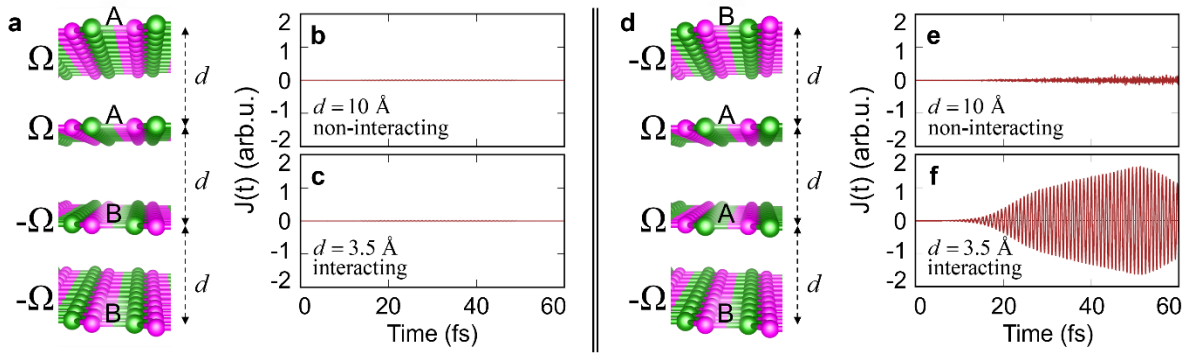

Figure 7. Role of interlayer distance in nonlinear Hall responses from RT-TDDFT calculations. a, The BBAA stacking geometry, where *d* denotes the interlayer distance. Panels **b** and **c** show the corresponding RT-TDDFT current density response when *d* = 10 and 3.5 Å, respectively. Panels **d-f** are the same as panels **a-c** for BAAB stacking.

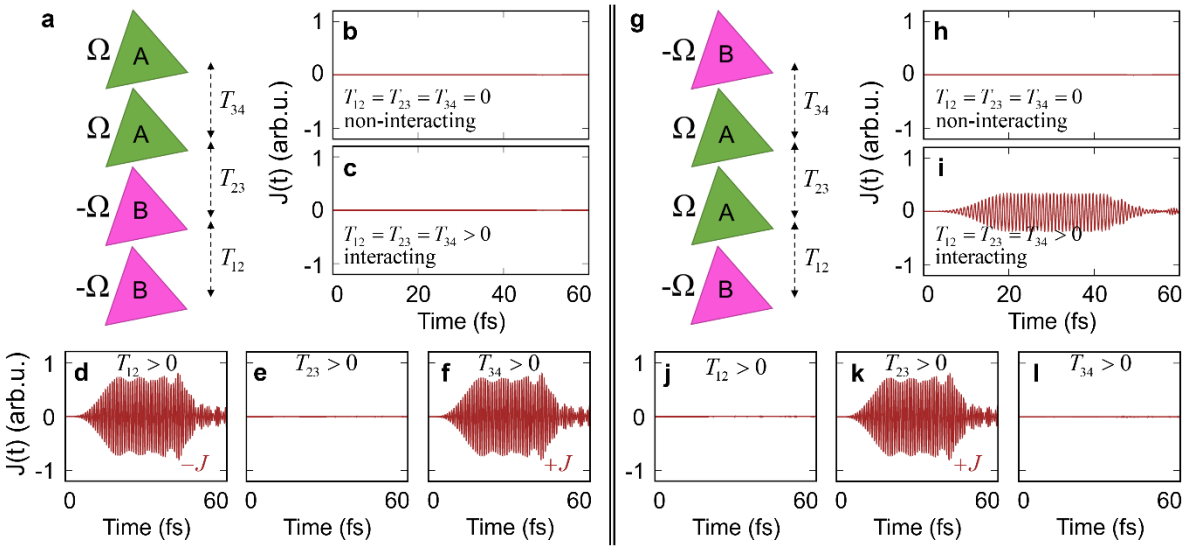

Figure 8. Analysis of interlayer interactions by tight-binding calculations. a, The BBAA stacking geometry, where the interlayer hopping parameters between 1st-2nd, 2nd-3rd, and 3rd-4th layers are T_{12}, T_{23}, and T_{34}, respectively. Panels **b-f** are the transverse current densities obtained from the model Hamiltonian calculations with the interlayer interactions as follows: **b**, no interaction: $T_{12} = T_{23} = T_{34} = 0$; **c**, full interaction: $T_{12} = T_{23} = T_{34} > 0$; **d**, only the bottom two layers interact: $T_{12} > 0$, $T_{23} = T_{34} = 0$; **e**, only the middle two layers interact: $T_{23} > 0$, $T_{12} = T_{34} = 0$; and **f**, only top two layers interact: $T_{34} > 0$, $T_{12} = T_{23} = 0$. Panels **g-l** are the same as panels **a-f** for BAAB stacking.

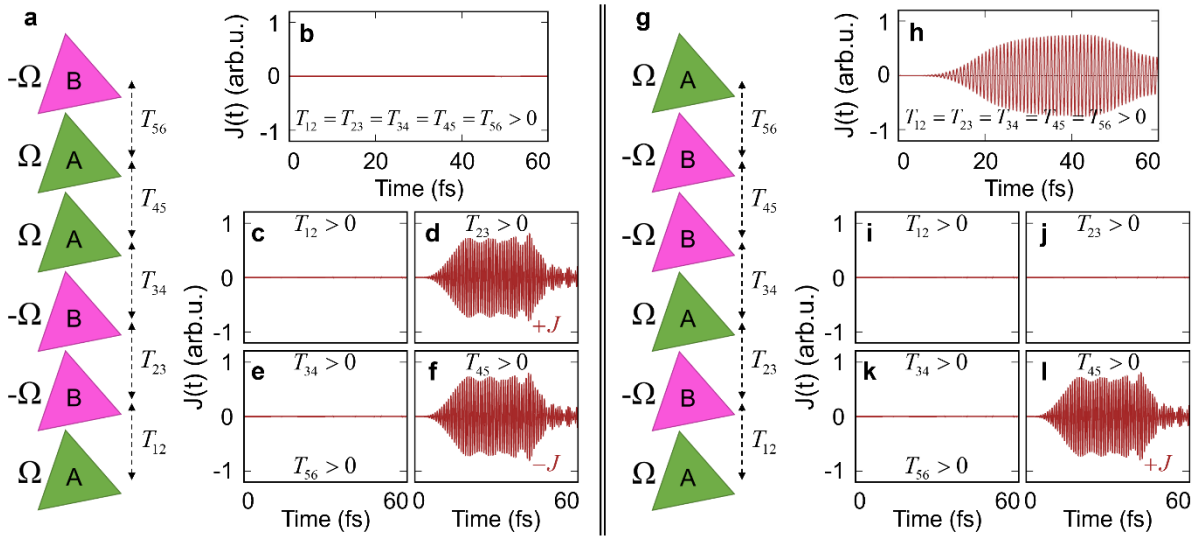

Figure 9. Analysis of interlayer interactions in 6-layer structures with tight-binding calculations. **a**, ABBAAB stacking geometry, where the interlayer hopping parameters between the 1st-2nd, 2nd-3rd, 3rd-4th, 4th-5th and 5th-6th layers are T_{12}, T_{23}, T_{34}, T_{45}, and T_{56}, respectively. Panels **b-f** depict the transverse current densities obtained from the model Hamiltonian calculations with the interlayer interactions as follows: **b**, all neighboring layers are interacting: $T_{12} = T_{23} = T_{34} = T_{45} = T_{56} > 0$; **c**, only the bottom two layers interact: $T_{12} > 0$; **d**, only the 2nd and 3rd layers interact: $T_{23} > 0$; **e**, only the 3rd and 4th layers interact: $T_{34} > 0$; and **f**, only the 4th and 5th layers interact: $T_{45} > 0$. The case where only the top layers interact, $T_{56} > 0$, exhibits the exact same result (zero) as **c** or **e**; thus, **e** is labeled with both $T_{34} > 0$ and $T_{56} > 0$. Panels **g-l** are the same as panels **a-f** for ABABBA stacking.

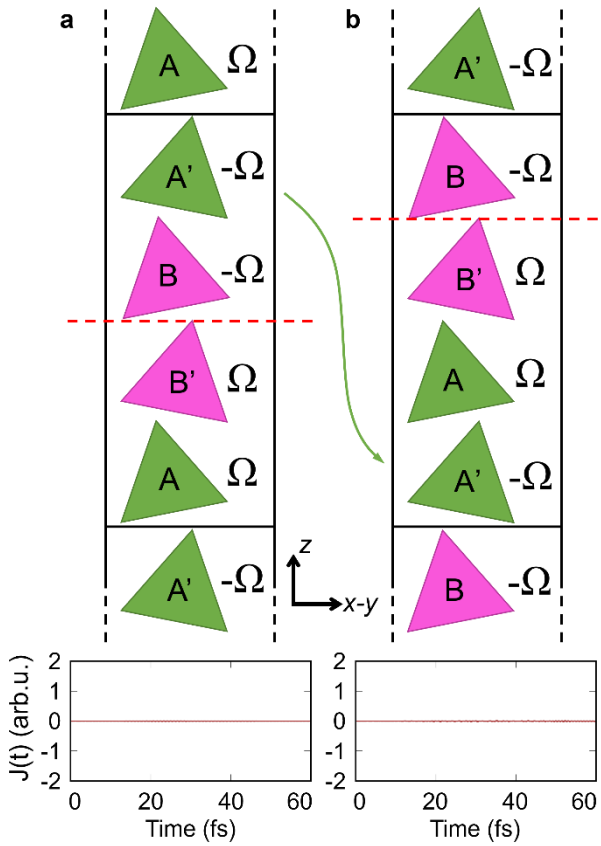

Figure 10. Real-time transverse second-harmonic optical responses of twisted h-BN bulk structures. The upper panels of **a** and **b** illustrate the bulk unit cells of AB'BA' and A'AB'B stackings, respectively. The dashed red lines represent the symmetry centers where the Berry curvatures of the layers are odd with respect to them. The lower panels are the current density response of the bulk structures obtained by RT-TDDFT calculations.